Geochemistry Geophysics Geosystems G3

Article
Volume 13, Number 1
25 October 2012
Q0AG12, doi:10.1029/2012GC004314
ISSN: 1525-2027

Published by AGU and the Geochemical Society

The cooling history and the depth of detachment faulting at the Atlantis Massif oceanic core complex

Nicole Schoolmeesters, Michael J. Cheadle, and Barbara E. John
Department of Geology and Geophysics, University of Wyoming, Dep. 3006, 1000 University Avenue, Laramie, Wyoming 82071, USA (nschoolmeesters@gmail.com)

Peter W. Reiners
Department of Geosciences, University of Arizona, Gould-Simpson Building #77, 1040 E. 4th Street, Tucson, Arizona 85721, USA

Jeffrey Gee
Scripps Institution of Oceanography, University of California, San Diego, 9500 Gilman Drive #0220, La Jolla, California 92093-0220, USA

Craig B. Grimes
Department of Geosciences, Ohio University, 316 Clippinger Laboratories, Athens, Ohio 45701, USA

[1] Oceanic core complexes (OCCs) are domal exposures of oceanic crust and mantle interpreted to be denuded to the seafloor by large slip oceanic detachment faults. We combine previously reported U-Pb zircon crystallization ages with (U-Th)/He zircon thermochronometry and multicomponent magnetic remanence data to determine the cooling history of the footwall to the Atlantis Massif OCC (30°N, MAR) and help establish cooling rates, as well as depths of detachment faulting and gabbro emplacement. We present nine new (U-Th)/He zircon ages for samples from IODP Hole U1309D ranging from 40 to 1415 m below seafloor. These data paired with U-Pb zircon ages and magnetic remanence data constrain cooling rates of gabbroic rocks from the upper 800 m of the central dome at Atlantis Massif as 2895 (+1276/−1162) °C Myr^{-1} (from ~780°C to ~250°C); the lower 600 m of the borehole cooled more slowly at mean rates of ~500 (+125/−102) °C Myr^{-1} (from ~780°C to present-day temperatures). Rocks from the uppermost part of the hole also reveal a brief period of slow cooling at rates of ~300°C Myr^{-1}, possibly due to hydrothermal circulation to ~4 km depth through the detachment fault zone. Assuming a fault slip rate of 20 mm/yr (from U-Pb zircon ages of surface samples) and a rolling hinge model for the sub-surface fault geometry, we predict that the 780°C isotherm lies at ~7 km below the axial valley floor, likely corresponding both to the depth at which the semi-brittle detachment fault roots and the probable upper limit of significant gabbro emplacement.

Components: 12,600 words, 6 figures, 2 tables.

Keywords: Atlantis Massif; oceanic core complex; oceanic detachment fault; zircon.

Index Terms: 1140 Geochronology: Thermochronology; 1744 History of Geophysics: Tectonophysics; 3035 Marine Geology and Geophysics: Midocean ridge processes.

Received 27 June 2012; **Revised** 21 September 2012; **Accepted** 24 September 2012; **Published** 25 October 2012.

Schoolmeesters, N., M. J. Cheadle, B. E. John, P. W. Reiners, J. Gee, and C. B. Grimes (2012), The cooling history and the depth of detachment faulting at the Atlantis Massif oceanic core complex, *Geochem. Geophys. Geosyst.*, *13*, Q0AG12, doi:10.1029/2012GC004314.

Theme: Oceanic Detachment Faults

1. Introduction

[2] Sixty percent of the present-day Earth's surface is created at mid-ocean ridges, yet, because of their relative inaccessibility, they remain one of the least understood tectonic features on the planet. The Mid-Atlantic Ridge (MAR) is a slow-spreading (2–3 cm/yr) mid-ocean ridge characterized by symmetrically spreading ridge segments with deep rift valleys, exhibiting bathymetric relief from 100's to 1000's of meters [*Small*, 1998] with new crust created by magmatic intrusion during plate separation. However, there are segments of the MAR where tectonic extension dominates over magmatic processes, causing asymmetric plate spreading, and formation of smooth, domal oceanic core complexes (OCCs) [e.g., *Blackman et al.*, 1998; *Tucholke et al.*, 1998; *Smith et al.*, 2006, 2008]. OCCs commonly form at the inside corner of ridge-transform intersections; examples include Atlantis Massif (MAR 30°N [*Cann et al.*, 1997; *Blackman et al.*, 1998, 2002, 2006, 2011; *Tucholke et al.*, 1998], the Kane OCC (MAR 23°N [*Dick et al.*, 2008]), and the Atlantis Bank OCC on the SW Indian Ridge [*Baines et al.*, 2008]. However, OCCs can form within a ridge segment, such as at the 13°N and 15°N segments of the MAR [*Kelemen et al.*, 2007; *Smith et al.*, 2006, 2008; *MacLeod et al.*, 2009], at the Trans-Atlantic Geotraverse (TAG) segment at MAR 26°N [*deMartin et al.*, 2007], at the B3 segment of the Australian-Antarctic Discordance [*Okino et al.*, 2004], and the Godzilla OCC in the Philippine Sea [*Ohara et al.*, 2001; *Tani et al.*, 2011].

[3] OCCs are high-standing domal exposures of oceanic lithosphere, including gabbro and mantle peridotite, exposed in the footwall of large-offset normal faults [*Cann et al.*, 1997; *Tucholke et al.*, 1998]. Similar structures, known as metamorphic core complexes, are found associated with extreme extension in continental settings [*Crittenden et al.*, 1980; *John*, 1987; *Davis and Lister*, 1988], including rifted continental margins [*Froitzheim and Manatschal*, 1996; *John and Cheadle*, 2010]. Acting as the plate boundary, oceanic detachment faults emerge at a low angle (<15°) from the axial valley, and likely steepen at depth to dips of ≥50–70° beneath the ridge axis [*Buck*, 1988; *Buck et al.*, 2005; *Garcés and Gee*, 2007; *deMartin et al.*, 2007; *Morris et al.*, 2009]. Documented slip duration along oceanic detachment faults is up to four million years [*John and Cheadle*, 2010; *Tani et al.*, 2011], leading to tectonic denudation of greater than ten kilometers of oceanic lithosphere (Figure 1). Locally, these detachment faults accommodate between 60 to 100% of plate spreading during periods of reduced magma supply [*Tucholke and Lin*, 1994; *Tucholke et al.*, 1998; *Grimes et al.*, 2008; *Smith et al.*, 2008]. The magma may be emplaced to form gabbro bodies in the footwall of the detachment fault [e.g., *Ildefonse et al.*, 2007; *Olive et al.*, 2010], but the proportion of diking and volcanism at the ridge axis is reduced compared to that at more normal, symmetrically spreading abyssal hill dominated ridge segments [*Buck et al.*, 2005; *Tucholke et al.*, 2008]. The relationship between where and how these detachment faults root however, and why they form and ultimately cease are still largely in question [*Tucholke et al.*, 2008; *MacLeod et al.*, 2009; *Olive et al.*, 2010; *Escartín and Canales*, 2011].

[4] Here, we present new (U-Th)/He zircon ages from drill core recovered from IODP Hole U1309D into the Atlantis Massif OCC, at 30°N on the MAR. The (U-Th)/He zircon cooling ages, combined with U-Pb zircon crystallization ages from *Grimes et al.* [2008] and multicomponent magnetic remanence data [*Blackman et al.*, 2006; *Morris et al.*, 2009, 2011], characterize the downhole cooling history of the OCC. We use these data to construct a cross-section detailing the thermal structure of the footwall of the Atlantis Massif OCC, establishing the depths of the 190°C and 780°C isotherms, and providing constraints on the temperature of the subsurface detachment fault and footwall. These data also provide an independent constraint on the

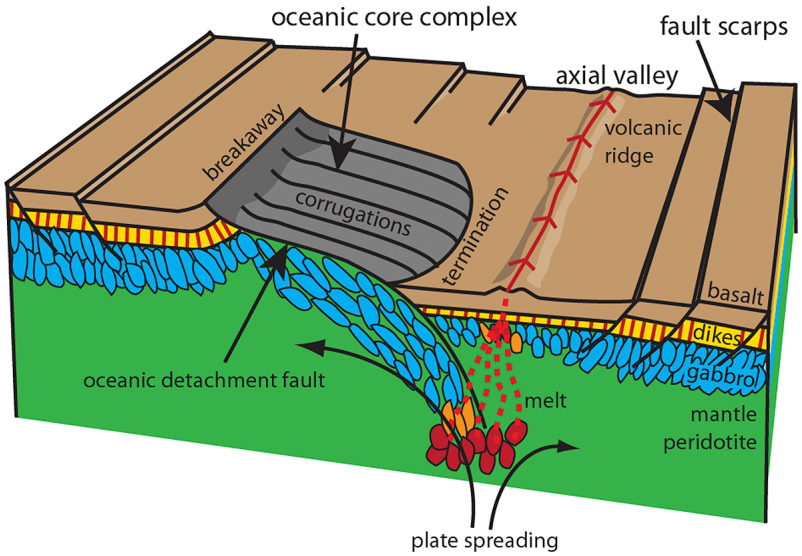

Figure 1. Cartoon of a slow-spreading ridge showing asymmetric plate spreading and associated formation of an oceanic core complex. Image highlights main attributes, including the breakaway – location where the oceanic detachment fault originally surfaced on the seafloor; spreading-parallel corrugations on the surface of the core complex; gabbro plutons within upper mantle peridotite denuded by the fault (red indicates recently intruded melt rich plutons, orange indicates partially crystallized plutons, and blue indicates fully solidified plutons); and the termination where the oceanic detachment fault dips below the axial valley. The detachment fault forms via a rolling hinge model, initially with a moderate-to steep dip beneath the rift valley and flattens as it emerges to the seafloor at the rift valley wall. Modified from *Grimes et al.* [2008] and *Escartín and Canales* [2011].

minimum depth at which the detachment fault roots beneath the axial valley, as well as the depth of significant gabbro emplacement.

2. Geology and Tectonic Setting of IODP Hole U1309D and Atlantis Massif, MAR 30°N

2.1. Atlantis Massif

[5] Atlantis Massif (MAR 30°N) forms an inside corner high at the eastern intersection of the slow spreading MAR and the Atlantis Transform Fault (Figure 2). The massif is approximately 75 km long by 15 km across, and consists of a Central Dome and a Southern Ridge [*Blackman et al.*, 2006]. The Central Dome is thought to comprise dominantly gabbroic rocks intruded into upper mantle peridotite [*Blackman et al.*, 2006; *Canales et al.*, 2008; *Drouin et al.*, 2009, 2010; *Blackman et al.*, 2011]. The gently sloping pillow basalt-covered ridge along the eastern flank of the dome is interpreted to be the hanging wall block to the detachment fault, delimiting the termination of the detachment surface [*Blackman et al.*, 2002, 2006; *Canales et al.*, 2008]. The corrugated surface of this OCC is inferred to be the footwall of the oceanic detachment fault, dipping ~5° west near the likely breakaway and rolling over to dip 12° east beneath the hanging wall [*Blackman et al.*, 2002; *Schroeder and John*, 2004; *Grimes et al.*, 2008]. *Canales et al.* [2008] identified two possible breakaways, or a breakaway zone, where the detachment fault initially cut the seafloor (Figure 2). Identification of a specific breakaway ridge is ambiguous at Atlantis Massif due to the hummocky nature of the volcanic layer on the seafloor and sedimentation that has occurred since the fault was exposed. However, the ridge defining breakaway 1 is more prominent than that defining breakaway 2, and accordingly, *Canales et al.* [2008] favored breakaway 1 for their detachment fault model; an interpretation which we follow in this work. They also identified the fault termination as the location where smooth, corrugated bathymetry interpreted as the fault surface is juxtaposed to the east against rough volcanic terrain of the hanging wall.

[6] The highstanding Southern Ridge forms part of the northern wall of the Atlantis Transform Fault (Figure 2) and reveals a cross section through the OCC [*Blackman et al.*, 2002; *Schroeder and John*, 2004; *Boschi et al.*, 2006; *Karson et al.*, 2006]. The Southern Ridge exposes the ~100 m thick detachment fault shear zone above dominantly

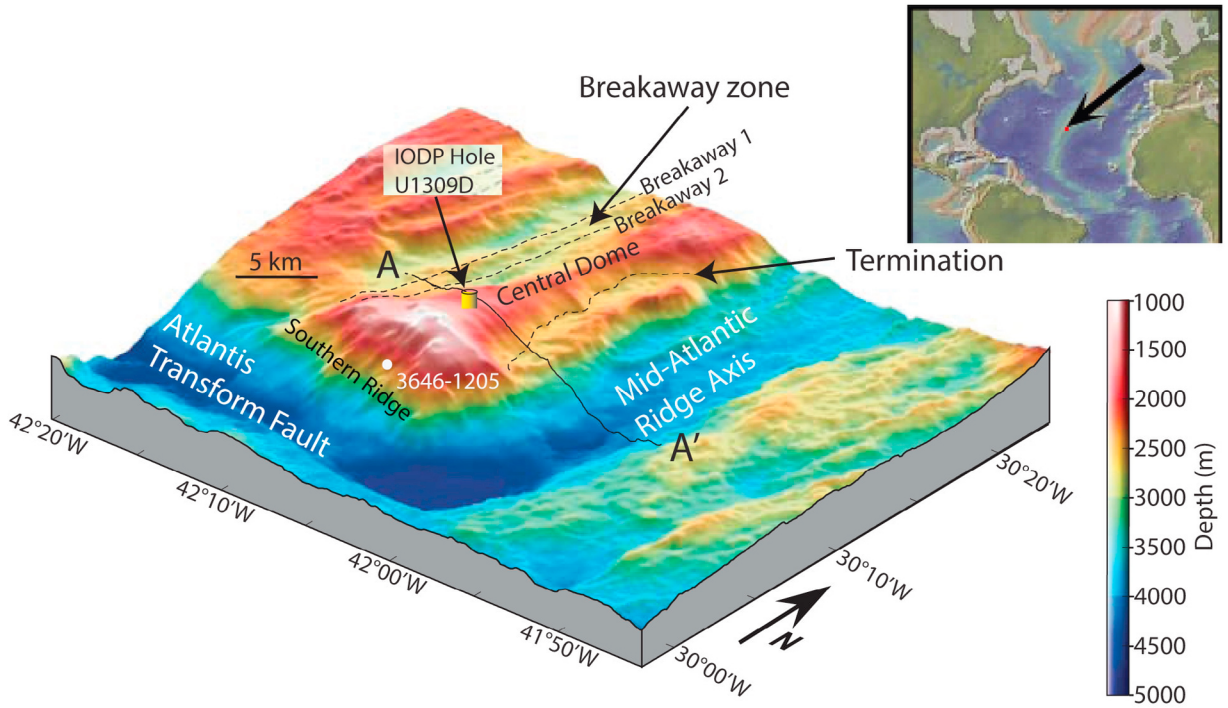

Figure 2. Bathymetric map of Atlantis Massif with dashed lines showing the breakaway zone and termination. Hole U1309D is indicated on the Central Dome. Location of dredge sample 3646–1205, referenced in this study, is shown on the Southern Ridge. Cross section line A-A′ is shown for Figure 5. Inset shows location of the Atlantis Massif on the MAR. Modified from *Canales et al.* [2008].

serpentinized peridotite with interfingering gabbroic bodies, and the Lost City hydrothermal field is hosted along this south wall scarp [*Kelley et al.*, 2001]. There the detachment fault/shear zone comprises greenschist facies talc-amphibole schists and mylonitic serpentinites, which are overprinted by brittle structures [*Blackman et al.*, 2002; *Schroeder and John*, 2004; *Boschi et al.*, 2006; *Karson et al.*, 2006]. At the location of IODP Hole U1309D, the detachment fault/shear zone is defined by a damage zone comprised of brittle to semi-brittle fracturing and intense alteration up to 100 m thick at the top of the footwall.

[7] The regional time-averaged symmetric half-spreading rate is ~12 mm/yr over the past 2 Ma [*Zervas et al.*, 1995], but asymmetric spreading has been inferred for the formation of OCCs based on U-Pb zircon and magnetic anomaly ages [*Baines et al.*, 2008]. At the Atlantis Massif OCC, *Grimes et al.* [2008] used U-Pb zircon ages to determine a spreading rate corresponding to the slip rate of the detachment fault of 28.7 ± 6.7 mm/yr between ~1.2 to 1.0 Myr. However, *Grimes et al.* [2011] argued that a reasonable estimate of the slip rate for the entire ~1.0 Myr duration of detachment faulting is 20 mm/yr and we prefer to use this more conservative estimate in this work, although we also discuss the effect of using a full spreading rate of 24 mm/yr. Using a 20 mm/yr spreading rate implies that the OCC was denuded at the seafloor between ~1.3–0.4 Ma.

2.2. IODP Hole U1309D

[8] In 2004/2005, the Integrated Ocean Drilling Program (IODP) Expedition 304/305 drilled several holes on the central dome of Atlantis Massif (Site U1309) in an effort to examine the nature of the detachment fault and the composition of the lithosphere in the footwall. IODP Hole U1309D (30°10.12′N, 42°07.11′W; 1645 mbsl), located ~14 km west of the present-day axial valley of the MAR, reached 1415 m into the footwall of the detachment fault bounding the OCC (Figure 2). Recovery from U1309D was ~75%, with the section composed of 92% gabbroic rocks, and a few percent residual mantle peridotite (~5%), younger intrusive diabase (~3%), and felsic dikes (<1%) (Figure 3a) [*Blackman et al.*, 2006, 2011; *Ildefonse et al.*, 2007; *John et al.*, 2009; *Drouin et al.*, 2009, 2010]. The gabbroic rocks range in composition from troctolites, troctolitic gabbro, olivine gabbro, gabbro, microgabbro/diabase, to Fe-Ti oxide gabbro. Typically the more evolved gabbros and felsic

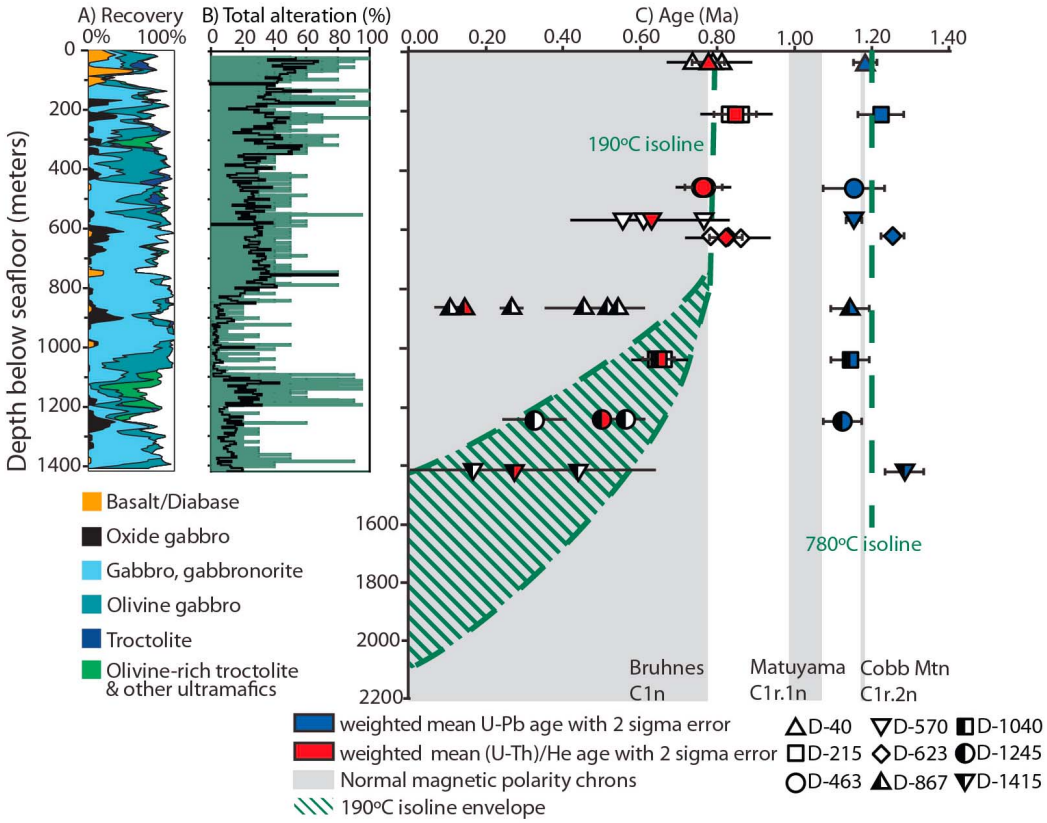

Figure 3. Downhole observations from IODP Hole U1309D at the Atlantis Massif OCC. (a) Plot showing a 20 m running average of recovery and rock composition/proportions down the hole (white = no recovery). (b) Plot showing overall alteration (in percent per core), with a 5 m running average represented by the black line. (c) Plot showing the weighted mean U-Pb zircon ages (blue symbols) and both individual and weighted mean (U-Th)/He zircon ages (white and red symbols, respectively) against depth (mbsf) in IODP Hole U1309D. The weighted mean U-Pb zircon age for all samples from the core is 1.20 ± 0.03 Ma [*Grimes et al.*, 2008], corresponding to a weighted mean Ti-in-zircon temperature of 780°C. This is shown as the green dashed 780°C isoline. Weighted mean (U-Th)/He zircon ages decrease downhole, with the exception of the much younger than expected He age of sample D-867. (U-Th)/He ages have closure temperatures that average 190°C, defining a 190°C isoline in the upper 800 m of the plot (green dashed line). Below 800 m in the plot a single 190°C isoline is hard to define, but the green-diagonally shaded area represents an envelope whose upper and lower boundaries pass through the youngest and oldest (U-Th)/He ages for samples D-1245 and D-1415, within which the 190°C isoline should lie. Grey boxes indicate normal magnetic polarity chrons from *Ogg and Smith* [2004]. Figures 3a and 3b are modified from *Blackman et al.* [2006].

dikes intrude into the more primitive gabbros. Diabase dikes are more common in the top 120 m of the hole, but are present sparingly (<1%) throughout the rest of the core, and were intruded during the faulting, cutting all rock types [*Blackman et al.*, 2006; *Grimes et al.*, 2008; *John et al.*, 2009]. The relatively small volume of these dikes means that the cooling histories of the samples were likely not significantly affected by the intrusion of the dikes, unless the sample was located very close to a dike.

[9] Overall, the alteration in the core ranges from heavy alteration (30–80%) in the top 300 m, moderate alteration (20–50%) to 800 m below the seafloor (mbsf), and only very localized alteration (5–20%) in the bottom of the core (Figure 3b) [*Blackman et al.*, 2006]. Greenschist facies alteration is widespread, and overprints higher-temperature granulite and amphibolite facies alteration in the upper part of the core. Zeolite facies assemblages are fairly abundant in fractures below 700 mbsf [*Blackman et al.*, 2006, 2011; *Karson et al.*, 2006; *McCaig et al.*, 2010].

3. Analytical Methods

3.1. Sampling

[10] The samples for U-Pb geochronology were chosen from representative depths down the core,

Table 1. Sample Rock Type, Depth (mbsf), Weighted Mean U-Pb Ages, and Ti-in-Zircon Temperatures[a]

IODP Name	Depth (mbsf)	Rock Type	Age[b] (Ma)	2 Sigma Error[b]	Ti-in-Zircon Temp[c] (°C)	Ti-in-Zircon Temp[d] (°C)	2 Sigma Variation
U1309D 5R3 136–144 cm	40	Plagioclase-amphibole vein intruding gabbro	1.18	0.03	692° (n = 18)	767°	50°
U1309D 40R1 21–25 cm	215	Trondjhemite	1.22	0.06	677° (n = 13)	753°	34°
U1309D 93R1 27–37 cm	463	Trondjhemite	1.15	0.08	714° (n = 10)	789°	87°
U1309D 115R2 59–67 cm	570	Oxide-bearing leucocratic zone intruding gabbro	1.15	0.02	701° (n = 9)	775°	68°
U1309D 126R2 27–38 cm	623	Fe-Ti oxide gabbro	1.25	0.03	685° (n = 12)	761°	78°
U1309D 178R1 97–102 cm	867	Leucocratic vein intruding gabbro	1.14	0.05	713° (n = 11)	788°	74°
U1309D 216R1 54–59 cm	1040	Trondjhemite	1.14	0.05	758° (n = 11)	833°	60°
U1309D 259R1 22–27 cm	1245	Fe-Ti oxide gabbro	1.12	0.05	717° (n = 12)	791°	72°
U1309D 295R3 100–110 cm	1415	Quartz diorite	1.28	0.05	748° (n = 8)	823°	74°

[a]mbsf = meters below seafloor. n = number of analyses.
[b]SIMS U-Pb zircon ages from *Grimes et al.* [2008].
[c]Ti-in-zircon temperatures with pressure correction [*Ferry and Watson*, 2007; *Ferriss et al.*, 2008].
[d]Ti-in-zircon temperatures without the pressure correction [*Ferry and Watson*, 2007].

based on the known occurrences of zircon in the more evolved gabbroic rock types – specifically Fe-Ti oxide gabbro and leucocratic veins [*Grimes et al.*, 2008]. Sample names used in the text are based on their depth of occurrence along the length of core (i.e., sample D-40 came from 40 mbsf in Hole U1309D; Table 1). Zircon grains used in this (U-Th)/He thermochronometric study came from three Fe-Ti oxide gabbro, and six leucocratic vein samples originally analyzed for U-Pb ages by *Grimes et al.* [2008] (Table 1). The choice of zircon grains for this study was constrained by morphology, size, zonation in cathodoluminescence (CL) imaging, and depth in the core. Specifically, zircon grains were chosen based on four visual criteria: 1) euhedral to subhedral grain shape, 2) a diameter of at least 80 μm in the shortest dimension, 3) few inclusions, and 4) lack of apparent zonation in CL.

[11] Grain mounts for secondary ion mass spectrometry (SIMS) analyses were imaged with CL, which can represent, qualitatively, a visual image of elemental distribution throughout a grain [*Hanchar and Miller*, 1993]. Young igneous zircons from oceanic gabbros typically display a flat gray appearance in CL with faint oscillatory zoning, suggesting fairly restricted zonation in uranium [see *Grimes et al.*, 2009].

3.2. (U-Th)/He Thermochronology

[12] The (U-Th)/He ages presented here were processed at the Arizona Radiogenic Helium Dating Laboratory (ARHDL) at the University of Arizona, following the methods of *Reiners* [2005]. Zircons were picked, imaged, and measured before being packed into 1 mm diameter niobium tubes; niobium is a malleable metal that acts as an oven for degassing of the grains. A CO_2 laser aimed at the niobium packet heated the sample for 15 min, effectively degassing the grain. Each sample was run through the lasing process twice, the second re-extract run insured that the grain was completely degassed. Molar concentrations of helium were analyzed using a quadrupole mass spectrometer. Each zircon and their niobium tubes were subsequently placed into microvials spiked with ^{233}U and ^{229}Th, and dissolved in a multistep HF-HNO_3-HCl mixture in dissolution bombs. Solutions were analyzed by high-resolution inductively coupled plasma mass spectrometry (HR-ICP-MS) to determine uranium and thorium contents.

[13] An alpha ejection correction was applied to the raw (U-Th)/He ages following *Reiners* [2005] (Table 2). Alpha particles can move up to ~20 μm when ejected from their parent isotopes during radioactive decay, so a correction is made to account for ^{4}He loss from the edges of each grain [*Farley et al.*, 1996]. Euhedral grains (tetragonal prism with 2 bipyramidal ends) are ideal, but the correction can be modified for grains missing pyramids [*Reiners*, 2005] or for polished grains extracted from grain mounts [*Reiners et al.*, 2007]. U-Th zonation in zircon also affects this correction [*Hourigan et al.*, 2005], but oceanic zircons typically have low concentrations of both uranium and thorium and often do not display strong zonation patterns in CL [*Grimes et al.*, 2009]. Analytical precision on individual measurements of isotopic ratios are typically 2% (1 sigma), however, zircon standards give a reproducibility error of 9%.

Table 2. (U-Th)/He Isotopic Ratios and Ages From Oceanic Zircons[a]

Sample ID	Mass (ug)	Half-Width (μm)	U (ppm)	Th (ppm)	Th/U	He (nmol/g)	Raw Age (Myr)	Analytical Error (2 sigma)	Ft[b]	Corrected Age (Myr)	2 Sigma Error Used[c]	Closure Temperature[d] (°C)
D-40-1	8.0	63.5	175	86	0.50	0.689	0.656	0.081	0.81	0.809	0.081	190
D-40-2	8.9	61.5	203	104	0.52	0.788	0.642	0.067	0.81	0.789	0.071	190
D-40-3	16.9	68.5	192	87	0.47	0.701	0.613	0.053	0.83	0.734	0.066	193
D-40 weighted mean								0.037		0.773	0.042	191
D-215-1	11.3	84.0	153	99	0.66	0.680	0.715	0.034	0.83	0.864	0.078	192
D-215-2	*4.8*	*66.0*	*135*	*78*	*0.59*	*1.446*	*1.744*	*0.085*	*0.77*	*2.261*	*0.203*	*186*
D-215-3	14.4	76.3	147	91	0.64	0.633	0.698	0.032	0.84	0.830	0.075	193
D-215 weighted mean								0.023		0.847	0.054	193
D-463-1	14.8	70.5	66	44	0.68	0.261	0.636	0.032	0.84	0.761	0.068	193
D-463-2	24.7	76.8	31	14	0.47	0.120	0.656	0.039	0.86	0.766	0.069	195
D-463 weighted mean								0.024		0.764	0.049	194
D-570-1	42.2	102.3	10	4	0.36	0.032	0.536	0.190	0.88	0.608	0.190	200
D-570-2	20.5	63.3	16	6	0.39	0.061	0.670	0.049	0.88	0.764	0.069	194
D-570-3	45.1	94.8	8	3	0.40	0.024	0.505	0.044	0.91	0.556	0.050	199
D-570 weighted mean								0.032		0.627	0.040	198
D-623-1	65.6	84.0	61	43	0.72	0.289	0.749	0.037	0.91	0.823	0.074	200
D-623-2	16.4	67.8	47	28	0.61	0.216	0.755	0.045	0.88	0.859	0.077	193
D-623-3	39.2	88.0	42	25	0.61	0.182	0.706	0.031	0.90	0.786	0.071	198
D-623 weighted mean								0.021		0.821	0.043	197
D-867-1	34.5	57.5	18	8	0.43	0.024	0.225	0.031	0.84	0.267	0.031	193
D-867-2	231.0	132.5	39	20	0.53	0.116	0.491	0.021	0.92	0.534	0.048	208
D-867-3	90.9	108.0	20	9	0.48	0.012	0.098	0.008	0.90	0.109	0.010	203
D-867-4	18.7	70.0	18	8	0.46	0.041	0.383	0.101	0.84	0.454	0.101	194
D-867-5	36.3	79.3	11	5	0.42	0.030	0.455	0.087	0.86	0.527	0.087	197
D-867 weighted mean								0.007		0.145	na	199
D-1040-1	105.1	159.8	94	59	0.64	0.338	0.579	0.030	0.91	0.635	0.057	206
D-1040-2	128.2	131.5	26	13	0.50	0.095	0.606	0.038	0.91	0.663	0.060	207
D-1040 weighted mean								0.023		0.649	0.041	206
D-1245-1	13.6	55.5	17	9	0.55	0.052	0.500	0.050	0.89	0.563	0.050	190
D-1245-2	8.4	54.8	16	8	0.54	0.026	0.272	0.083	0.83	0.327	0.083	188
D-1245 weighted mean								0.043		0.501	na	189
D-1415-1	1.6	26.0	26	18	0.74	0.021	0.127	0.163	0.77	0.165	0.163	175
D-1415-2	3.6	37.3	16	11	0.72	0.035	0.343	0.202	0.78	0.439	0.202	181
D-1415-3	*2.9*	*33.5*	*16*	*10*	*0.63*	*na*	*−0.006*	*0.115*	*1*	*na*	*na*	*180*
D-1415 weighted mean								0.127		0.273	na	178

[a]Italicized analyses are interpreted to be inaccurate, see text for explanations.
[b]Ft is the alpha ejection correction applied to the raw age.
[c]2 sigma error used is the larger of either the analytical error or the reproducibility error.
[d]Closure temperature calculated using diffusion parameters from *Reiners et al.* [2004], *Guenthner et al.* [2011], and equation from *Dodson* [1973].

[14] Based on He diffusion data from *Reiners et al.* [2002, 2004] and empirical observations from boreholes and exhumed crustal blocks [*Stockli*, 2005; *Wolfe and Stockli*, 2010], He diffusion in zircon likely has an activation energy (E_a) of about 170 kJ/mol and a frequency factor (D_o) of about 0.5 cm^2/s, yielding a closure temperature of about 180°C for a cooling rate of ~10°C Myr^{-1}. Recent work by *Guenthner et al.* [2011], however, indicates that helium diffusivity in zircon with little radiation damage can be higher, primarily through an increased frequency factor. From these experiments and the extent of radiation damage inferred for young zircon studied here, we used an activation energy of 168 kJ/mol and a frequency factor of 16.2 cm^2/s. Combined with cooling rates of ~200–400°C Myr^{-1} as inferred from magnetic properties [*Morris et al.*, 2009] and from the findings of this study, this results in an average closure temperature of 190 ± 20°C (Figure 3c and Table 2). At these rapid cooling rates, closure temperature does not vary strongly with cooling rate. For example, changes of 100°C Myr^{-1} only cause ~2°C differences in helium closure temperatures.

3.3. SIMS U-Pb Ages

[15] Weighted mean U-Pb zircon SIMS ages for a suite of 18 samples from IODP Hole U1309D were previously reported by *Grimes et al.* [2008]. Table 1 lists the ^{238}U-^{230}Th disequilibrium corrected U-Pb ages of the samples chosen for (U-Th)/He dating in this study.

3.4. Ti-in-Zircon Thermometer

[16] *Grimes et al.* [2009] report titanium concentrations in zircon for six of the samples analyzed (D-40; D-215; D-463; D-570; D-1040; D-1415). We present titanium concentrations for the other three samples (D-623; D-867; D-1040) in Table S1 in the auxiliary material, which together, allow the temperatures of zircon crystallization to be estimated using the Ti-in-zircon thermometer [*Watson et al.*, 2006; *Ferry and Watson*, 2007; *Fu et al.*, 2008; *Ferriss et al.*, 2008].[1] Titanium activity is estimated to be 0.7, because rutile is not present in any of the samples. Quartz is observed in the leucocratic veins, indicating a silica activity of 1 for samples D-40, D-215, D-463, D-867, D-1040, and D-1415; we use a silica activity of 0.7 for the quartz-absent Fe-Ti oxide gabbro samples (D-570, D-623, D-1245). Changes in the titanium activity from 0.7 to 1 will decrease temperatures <40°C, while changes in the silica activity from 1 to 0.7 will decrease temperatures <40°C.

[17] Table 1 presents both the pressure uncorrected temperatures using the Ti-in-zircon thermometer of *Ferry and Watson* [2007] and the pressure corrected temperatures using the pressure correction of *Ferriss et al.* [2008]. This 10°C/kbar correction was applied to all samples, as the crystallization pressure of the rocks (~2.5 kbar) is lower than the pressure of the calibration experiments (10 kbar) for this thermometer [*Ferriss et al.*, 2008]. Consequently, this correction reduces the calculated *Ferry and Watson* [2007] mean temperatures by 75°C; for example from 776°C to 701 ± 42°C for the oxide gabbros. Unfortunately, these 'corrected' temperatures are significantly below the likely solidus temperature of 860 ± 30°C for igneous amphibole-bearing gabbro based on amphibole mineral chemistry [*Coogan et al.*, 2001] and below the closure temperature for lead diffusion in zircon from experimental studies (~850°C ± 50°C [*Cherniak and Watson*, 2003]). Therefore, we use the higher, uncorrected (for pressure) temperatures for the three oxide gabbro samples, which are close, after accounting for errors, to the solidus temperature of the gabbros reported by *Coogan et al.* [2001]. Accordingly, we also use the uncorrected (for pressure) temperatures derived from Ti-in-zircon thermometry to estimate the solidus temperatures for the six leucocratic vein samples (Table 1).

[18] Ranges in Ti-in-zircon temperatures for some samples are likely a consequence of the evolving chemistry of the crystallizing melt and the actual range of temperatures over which the zircon crystallized. Between 8 and 18 trace element analyses from multiple zircon grains were collected from each sample to generate a representative temperature range for zircon crystallization within each rock (Table S1) [*Grimes et al.*, 2008, 2009]. From these data, the weighted mean temperature is interpreted to correspond to the mean U-Pb crystallization age of the rock (Table 1). Mean temperatures for the leucocratic veins range from ~753 to ~833°C, and mean temperatures for the oxide gabbros range from ~761 to ~791°C. As these temperature ranges overlap, we use a weighted mean temperature of 780 ± 20°C when discussing the samples in general.

3.5. Paleomagnetic Data

[19] The age constraints from magnetic chron data [*Ogg and Smith*, 2004] and unblocking

[1] Auxiliary materials are available in the HTML. doi:10.1029/2012GC004314.

temperatures of multicomponent magnetic remanence data [*Morris et al.*, 2009] provide intermediate time and temperature constraints between the U-Pb and (U-Th)/He ages. Detailed thermal demagnetization [*Morris et al.*, 2009] reveals the presence of up to three remanence components in the core: 1) a high temperature reversed component (R1), 2) an intermediate temperature normal polarity component (N1), and 3) a lower temperature reversed component (R2). All three components are found in some samples from the upper 400 m of the core, with deeper samples having only the R1 and N1 or just the R1 components [*Morris et al.*, 2009]. The timing of these remanence components can be correlated with the magnetic chrons [*Ogg and Smith*, 2004] using the U-Pb crystallization age of the samples [*Grimes et al.*, 2008] as a reference. Five of the nine samples have U-Pb ages that lie within the C1r.2r chron (1.072–1.173 Ma) and are therefore younger than the brief normal Cobb Mtn. chron (C1r.2n; 1.173–1.185 Ma). We argue that the other four samples, with U-Pb ages older than the Cobb Mtn. chron, did not record this brief normal chron since the highest temperature magnetization component is reversed for all samples. Consequently, we suggest the R1 component was acquired between crystallization of the gabbro and the end of the C1r.2r chron (1.072–1.173 Ma); the N1 component was acquired during the Jaramillo normal chron (C1r.1n; 0.988–1.072 Ma); and the R2 component was acquired during the Matuyama reversed chron (C1r.1r; 0.781–0.988 Ma).

[20] For samples with sufficiently fine-grained (single-domain-like behavior) magnetite and multiple remanence components, the unblocking temperatures can provide additional information on the temperature at the magnetic polarity boundaries [*Gee and Meurer*, 2002]. The lowest laboratory unblocking temperature for the R1 component provides an upper limit for the temperature at the beginning of Chron C1r.1n; and the lowest unblocking temperature for the N1 component provides an upper limit for the temperature at the beginning of Chron C1r.1r. However, in the naturally cooled samples, longer cooling times likely mean the true unblocking temperatures are lower than those observed in the laboratory, and so temperature estimates therefore need to be revised downward to account for this time dependence. Following the methodology outlined by *Gee and Meurer* [2002], the laboratory derived 475–500°C lower bound for R1 could reflect in situ, true temperatures as low as 405–445°C at 1.072 Ma. Similarly, the laboratory derived ~300°C lower bound for the N1 component could have been produced by extended exposure to temperatures as low as 165°C as the rocks were denuded by the detachment fault. The magnetic data therefore suggest temperature bounds of 405–500°C at 1.072 Ma and 165–300°C at 0.988 Ma, with temperatures most plausibly being near the lower end of these ranges.

4. Results

4.1. (U-Th)/He Thermochronology Results

[21] Two to five zircon grains from each sample (whole grains if available, and if not, partly polished grains plucked from grain mounts) were individually analyzed (Table 2). For four samples (D-40, D-463, D-623, D-1040), individual (U-Th)/He grain ages were within error of others from the same sample. The other five samples have some grains with (U-Th)/He ages that do not overlap the ages of other grains from the same sample, within a 2-sigma error. These five samples are discussed in the remainder of this section.

[22] Grain 2 from sample D-215 (Table 2) was significantly smaller than the other two grains from this sample and gave a He age older than the U-Pb age. We suspect this grain may have been affected by He implantation from adjacent grains or some other sample-related problem, so it is not included in calculating the weighted mean (U-Th)/He age of sample D-215. All three single grain analyses for sample D-570 (Table 2) show a large variation in age and analytical error. The scattered ages partially result from low uranium (<16 ppm) and thorium (<6 ppm) concentrations (Table 2) in these grains. However, the weighted mean age was calculated using all three grains because the age and corresponding analytical error for grain 1 encompassed those of grains 2 and 3.

[23] Zircon from the two deepest samples, D-1245 and D-1415, were plucked from grain mounts and interpreted using a modified alpha ejection corrections, as partial grains were analyzed [*Reiners et al.*, 2007]. All five grains had He contents that are among the lowest in these samples; grain 3 from D-1415 had no measurable helium (Table 2). The low He and scattered dates are consistent with recent slow cooling likely indicating that the deep parts of Hole U1309D may have still been at temperatures close to 190°C within the last few tens of thousands of years. This suggestion is consistent with very recent downhole measurements in U1309D indicating a bottom hole temperature of ≥145°C [*Expedition 340T Scientists*, 2012].

[24] Five grains from sample D-867 were analyzed on two separate occasions because the sample

produced a large variation in age; all ages are younger than expected when compared to the (U-Th)/He ages of samples above and below, with a weighted mean He age of 0.145 Ma (Table 2). Even the oldest grain from sample D-867 is almost 100 kyr younger than weighted mean He age of 0.649 Ma for the closest sample (D-1040) in the core. There are no obvious textural or petrographic features in these grains to account for these anomalously young ages. We speculate that the age dispersion may have been caused by a nearby thermal event that partially reset He ages some time since 0.5 Ma. Unfortunately, there is no obvious evidence in the core for this thermal event; this part of the core has excellent recovery (90 to 95%) and limited alteration (10 to 30%). The nearest diabase dike recovered is 4 m away and is only a few centimeters thick [*John et al.*, 2009]. However, it is possible that a thermal event was caused by a late intrusion or by hydrothermal activity along an adjacent fault that are close to, but do not cut, the borehole, and hence are not seen in the core.

4.2. U-Pb and (U-Th)/He Age Depth Profile

[25] *Grimes et al.* [2008] reported U-Pb zircon ages for the samples analyzed in this study and found only a small, but random, age variation of <200 kyr with depth. The weighted mean U-Pb zircon age of the core is 1.20 ± 0.03 Ma, and the corresponding weighted mean Ti-in-zircon temperature is 780 ± 20°C, which together define a temperature isoline in Figure 3c (Table 1). As might be expected, the (U-Th)/He zircon ages young downhole (Figure 3c). In the top 650 m of Hole U1309D, the (U-Th)/He zircon ages average 0.75 Ma and steadily decrease in age downhole to 0.27 Ma at 1415 m depth. The one exception is sample D-867 (discussed above), which shows an out of sequence, anomalously young age of 0.145 Ma. The (U-Th)/He closure temperatures for the samples analyzed average 190°C (Table 2) and define an additional temperature isoline in Figure 3c.

[26] The relatively small number of samples, taken with the large variation in He ages for grains from samples D-1245 and D-1415 (Table 2), means that there is some uncertainty in the position of the 190°C isoline in the lower part of Figure 3c. The green-diagonally shaded area in Figure 3c is an envelope whose upper and lower boundaries pass through the youngest and oldest (U-Th)/He zircon ages for samples D-1245 and D-1415. Extrapolation of the shaded area to zero age therefore constrains the present-day 190°C temperature to lie between 1450 mbsf and 2000 mbsf, consistent with recent relogging of IODP Hole U1309D, which recorded a minimum temperature of 145°C at 1415 m [*Expedition 340T Scientists*, 2012]. This leads to a predicted present-day geothermal gradient of ~102–135°C/km.

5. Discussion

5.1. Cooling History Curves

[27] Thermochronometric data for each sample are plotted in Figure 4, with additional temperature-age constraints provided by paleomagnetic remanence data from IODP Hole U1309D. The U-Pb zircon ages and Ti-in-zircon temperatures provide estimates of the age and temperature for final crystallization of the Fe-Ti oxide gabbros and/or leucocratic dikes. The (U-Th)/He ages and helium closure temperatures provide the low temperature constraints on the cooling histories for each sample. Additional constraints are provided by the present-day borehole temperature log, which recorded a minimum temperature of 145°C at 1415 mbsf [*Expedition 340T Scientists*, 2012], and by the extrapolation of the 190°C isoline derived from the He closure temperatures to zero age (Figure 3c). The measured bottom-hole temperature is considered to be a minimum because relogging could have disrupted the thermal structure at the bottom of the hole. We have also used our estimates of the present-day linear geothermal gradient (102–135°C/km) to predict the present-day temperature for each sample down the core. Intermediate temperature-age constraints on the cooling history are provided by the unblocking temperatures of multicomponent magnetic remanence [*Morris et al.*, 2009, 2011], discussed in section 3.5, together with age constraints from magnetic chron data [*Ogg and Smith*, 2004].

[28] The likely cooling history for each sample is shown in Figure 4, with cooling curves shown to pass through each thermochronometric constraint, assuming monotonic cooling. All samples show at least one reversed component of magnetic remanence, which when taken with the many zircon U-Pb ages <1.178 Ma, suggests that this magnetization was likely acquired during the C1r.2r chron (1.072–1.173 Ma). All cooling curves are therefore constrained to pass through the Curie temperature (~580°C) during this chron (shown by the yellow bar on all plots in Figure 4). The two samples from the shallow part of Hole U1309D (D-40 and D-215) have the best-constrained cooling curves. Samples

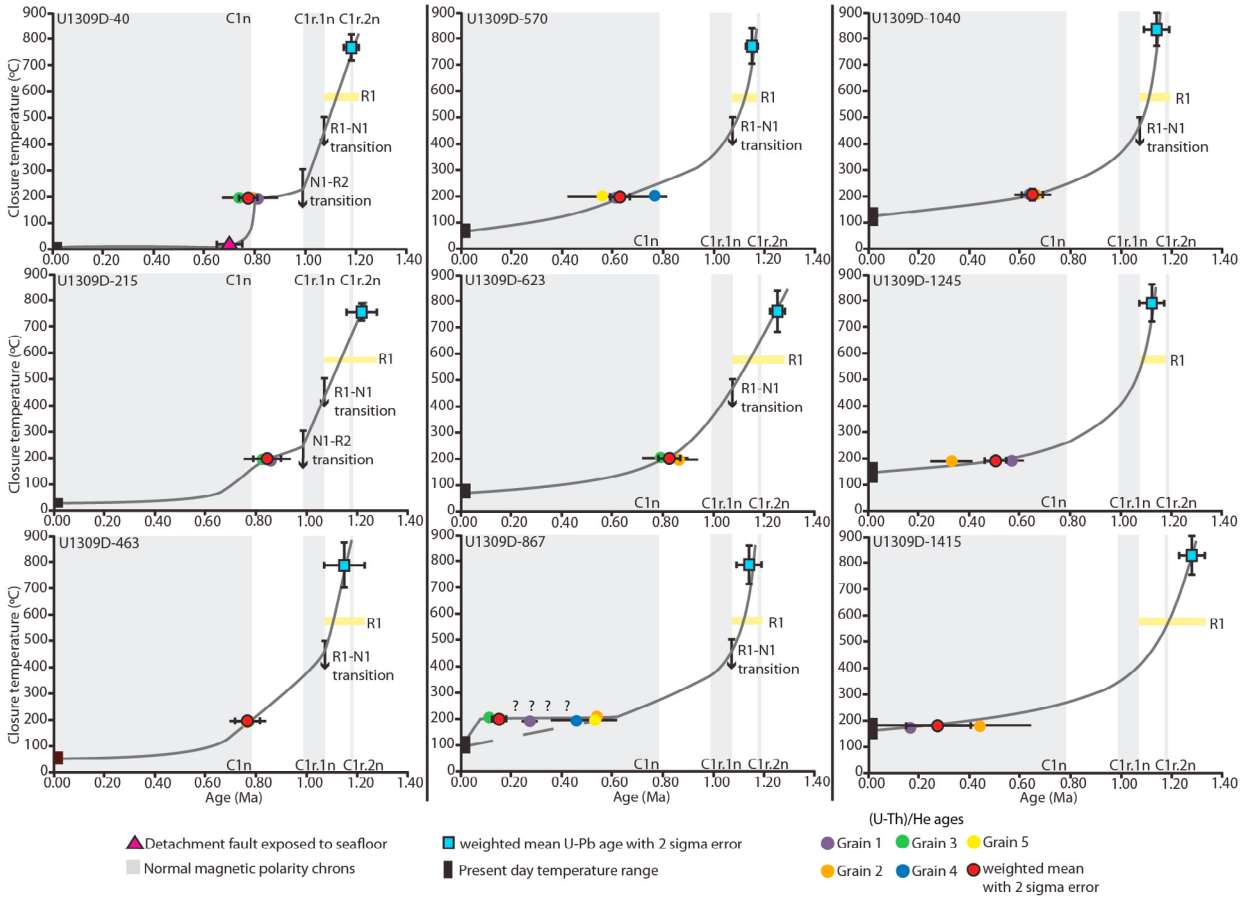

Figure 4. Temperature-age plots showing thermochronometric data for the samples from Hole U1309D. Blue squares are the weighted mean U-Pb zircon ages and corresponding Ti-in-zircon temperatures [*Grimes et al.*, 2008; this study]. Horizontal yellow bars and vertical arrows indicate temperature and age estimates from multicomponent magnetic remanence [*Morris et al.*, 2009]. Colored circles are the (U-Th)/He zircon ages and closure temperatures from this study; both single grain and weighted mean ages are plotted. Black bars along the *y* axis convey the uncertainty in present-day temperatures downhole. Grey regions indicate normal polarity magnetic chrons [*Ogg and Smith*, 2004]; white regions indicate reversed polarity chrons. Grey lines indicate a best fit cooling curve through each constraining point for each sample; dashed line for D-867 indicates expected cooling curve for this sample.

from the upper 450 m of the core commonly show two magnetic reversals in their multicomponent remanence data [*Morris et al.*, 2009], which provide two additional limits on the cooling curves. These curves indicate initial rapid mean cooling rates of 2895 (+1276/−1162) °C Myr^{-1} from 780°C to ∼250°C. Below this temperature, cooling apparently decreases dramatically between ∼250°C and 190°C to ∼300°C Myr^{-1}. This change in cooling rate is constrained by the estimated true unblocking temperature of between 300 and 165°C at the transition from the normal to reverse remanence component at the end of the Jaramillo chron (0.988 Ma [*Ogg and Smith*, 2004]) and this apparent "plateau" in the cooling curve is further discussed in the later section 5.4 (Implications for Hydrothermal Circulation).

[29] As the footwall is unroofed, temperatures in the uppermost part of Hole U1309D must approach 0°C, the approximate temperature of ocean water at the seafloor, which requires rapid cooling (∼2000°C Myr^{-1}) from 190°C at ∼0.80 Ma. This constraint is also consistent with the unblocking temperatures of the R2 magnetic component at 0.781 Ma, which extend down to temperatures of 100°C [*Morris et al.*, 2009]. The cooling history of the most shallow sample (D-40) is further controlled by the timing of the emergence of IODP Hole U1309D in the footwall to the seafloor at ∼0.70 Ma. Based on the present-day bathymetry, Hole U1309D lies 5.6 km west of the termination; using the fault slip rate of 20 mm/yr implies that the top of Hole U1309D reached the surface 0.28 Myr

before the fault stopped slipping. The distance from the termination of the fault to the axial valley wall is ~5.0 km. Assuming the spreading rate was equivalent to the half spreading rate of 12 mm/yr [*Zervas et al.*, 1995] after detachment faulting ceased, then detachment faulting likely stopped ~0.42 Myr ago. Combining these two ages gives an estimate of 0.70 Ma for the time the crust hosting Hole U1309D emerged at the seafloor.

[30] The five successively deeper samples (D-463, D-570, D-623, D-867, D-1040) have temperature-age constraints provided by the two thermochronometers used in this study, in combination with the predicted present-day temperature recorded in the borehole. Each of these samples also record one field reversal from reverse to normal, corresponding to the start of the Jaramillo chron (1.072 Ma [*Ogg and Smith*, 2004]). This constraint leads to initial cooling rates of ~2500°C Myr^{-1}, similar to those for the uppermost samples. Samples D-570, D-867, and D-1040 have younger (U-Th)/He ages than D-40, D-215, and D-623, implying slower cooling rates at temperatures below 450°C. The overall mean cooling rate for the samples from the top 800 m of the core is ~1500°C Myr^{-1} from 780°C to 190°C, consistent with the rate estimated by *Grimes et al.* [2011] for a single sample from the surface of Atlantis Massif (Alvin dive sample 3646–1205).

[31] The two deepest samples (D-1245 and D-1415) have the fewest constraints on their cooling curves (Figure 4). Only a single reversed component of magnetic remanence is found in the bottom 300 m of IODP Hole U1309D, indicating that this part of the core cooled below 580°C before the start of the Jaramillo chron (1.072–0.988 Ma [*Ogg and Smith*, 2004]). This limitation suggests that sample D-1245, at least, initially cooled at a rate of ~2500°C Myr^{-1}, similar to rates for samples from the top of the Hole U1309D. However, the very young (U-Th)/He ages relative to the rest of the samples and the present-day bottom hole temperature of >145°C requires slow average cooling rate between ~300 and 450°C Myr^{-1} below 580°C. The overall average cooling rate for these two samples is ~500°C Myr^{-1} from ~780°C to present-day temperatures.

5.2. Geometry of the Detachment Fault

[32] Oceanic detachment faults likely form at moderate-to-high angles (≥60°) and roll over flexurally to more gentle dips (0–20°) through time and progressive slip [e.g., *Buck et al.*, 2005; *Tucholke et al.*, 2008; *MacLeod et al.*, 2009; *John and Cheadle*, 2010; *Escartín and Canales*, 2011]. Four lines of evidence support the 'rolling hinge' model [*Buck*, 1988; *Wernicke and Axen*, 1988] for OCCs: mathematical models, microseismicity data, paleomagnetic data from drill cores, and seafloor bathymetry.

[33] Mathematical models [e.g., *Buck et al.*, 2005] predict long-lived detachment faults that initiate at moderate- to steep dips and rollover to gentle angles through time as a consequence of the reduced elastic thickness (~1 km) of oceanic lithosphere at a mid-ocean ridge [*Smith et al.*, 2008; *Schouten et al.*, 2010]. Evidence for active, steeply dipping normal faults and the rolling hinge model also comes from microseismicity data collected from the Trans-Atlantic Geotraverse (TAG) segment at 26°N, MAR. *DeMartin et al.* [2007] used microseismic events to delimit the geometry of a curviplanar fault that dips at ~70° at depths from 3 to 7 km below the seafloor, in conjunction with seismic tomographic data, to suggest that the fault rolls over to low dip angles (15–20°) with denudation of the crust. Other microearthquake studies at slow-spreading mid-ocean ridges have also recorded seismicity along steep faults from 5 to 8 km depths below seafloor [*Toomey et al.*, 1985, 1988; *Kong et al.*, 1992; *Wolfe et al.*, 1995].

[34] Paleomagnetic remanence data from samples recovered from OCCs also indicate a minimum of ~45° of tectonic rotation at temperatures below the onset of magnetization in oceanic crust (~580°C), consistent with active high angle faulting and the rolling hinge model. *Morris et al.* [2009] reoriented samples spanning the entire length of IODP Hole U1309D using high temperature, reversed components of magnetic remanence, and show the oceanic detachment fault at Atlantis Massif rotated 46° ± 6° anticlockwise along an axis trending roughly parallel to the present-day ridge axis. Using similar methods at drill sites from the Fifteen-Twenty Fracture Zone on the MAR, *Garcés and Gee* [2007] report tectonic rotation of 50–80°, and *MacLeod et al.* [2011] independently estimate the rotation of 64° ± 11° on the 15°45′N (MAR) OCC detachment fault.

[35] Finally, *Smith et al.* [2008] used the bathymetry (and slope) of the breakaway ridge to estimate the initial dip of the detachment system at the seafloor, also supporting the rolling hinge model. *Hansen et al.* [2007], *Smith et al.* [2008], and *MacLeod et al.* [2009] all calculate initial fault dips of 40–60° for breakaway faults at the Kane OCC and at 13°N on the MAR using this method.

5.3. Constructing the Thermal Structure of Atlantis Massif

[36] We use the thermochronometric, paleomagnetic, and downhole logging data from IODP Hole U1309D to predict the depth of isotherms in the footwall and hence develop a model for the thermal structure of the Central Dome of the Atlantis Massif OCC. The core recovered by IODP Hole U1309D can be thought of as a "temperature-probe" that records the thermal structure of the Central Dome as it moved from deep below the axial valley to its present-day location. We can invert the temperature-time data recorded by the core into the temperature-depth structure of the footwall by making three simple assumptions: 1) the sub-surface geometry of the fault, and therefore the trajectory of the core/footwall is known; 2) the footwall of the OCC had a steady state thermal structure during denudation; and 3) the slip rate of the detachment fault is known and hence the core moved at a known velocity through the temperature fields of the footwall.

[37] As discussed in section 5.2, the fault likely has a convex upwards geometry consistent with a rolling hinge model. Robust constraints on the dip of the fault at depth are provided by the paleomagnetic data of *Morris et al.* [2009]; the rotation recorded by these data limits the now horizontal fault (at Hole U1309D) to have had a dip of 46° ± 6° at the 580°C isotherm. *Morris et al.* [2009] also suggest that the mean direction of R1 and N1 magnetic remanence components for the top 400 m of the core are statistically antipodal and therefore conclude that the majority of the footwall rotation occurred after the acquisition of the N1 component. This interpretation constrains the fault to be planar between at least the 300°C (the upper temperature limit for the N1-R2 transition) and 580°C isotherms and are therefore likely planar to the 780°C isotherm.

[38] The difference between thermochronometric and paleomagnetic age estimates for each sample can be converted into a distance between isotherms in the footwall if the time-averaged slip rate is known as discussed above. For example, the difference between the U-Pb and the (U-Th)/He ages multiplied by the time averaged velocity of the footwall determines the distance between the 780°C and the 190°C isotherms in the upper 1.4 km of the OCC. Here, as discussed in section 2.1, we use a time-averaged velocity of 20 mm/yr constrained by age-distance relations derived from U-Pb zircon crystallization ages of samples from the surface of Atlantis Massif [*Grimes et al.*, 2008]. These data suggests that the slip rate was constant at a time scale of 50 kyr for at least the period of time from 1.2 to 1.0 Myr. Our assumption of a steady state thermal structure is supported by the similarity in cooling histories of the most shallow samples from IODP Hole U1309D and the surface sample 3646–1205 reported in *Grimes et al.* [2011], despite a 0.13 Myr difference in U-Pb ages.

[39] However, one additional constraint is required to "pin" or reference the isotherms relative to the seafloor. *Grimes et al.* [2011] argued that the 200°C isotherm at the detachment fault surface occurs at 1.5 km below the seafloor based on thermal and seismological models [*Phipps Morgan and Chen*, 1993; *Maclennan et al.*, 2005; *Canales et al.*, 2007], and used this as a reference depth for all other isotherms. Another method to "pin" the isotherms is to use the time that the crust hosting Hole U1309D core emerged at the seafloor; if that age is known, the depth to the 190°C isotherm at that time can be simply read from Figure 3c. In section 5.1 we argue that IODP Hole U1309D emerged at the seafloor ∼0.70 Myr ago, and examination of Figure 3c indicates that the core had a temperature of 190°C at ∼1.0 km depth at this age. This estimate is not significantly different to *Grimes et al.* [2011] estimate of 1.5 km depth for the 200°C isotherm. Figure 3c shows that an uncertainty as large at ±100,000 yr for the timing of Hole U1309D reaching the seafloor leads to a depth uncertainty of only ±200 m for the 190°C isotherm.

[40] This estimate for the depth below the seafloor of the 190°C isotherm is required as a reference point to determine the position of the other isotherms (780°C, 580°C, 450°C, and 250°C). Given the differences in age between the 190°C and 780°C isotherms and the 20 mm/yr fault slip rate, we predict that the 780°C isotherm was ∼8 km below the 190°C isotherm along the fault plane. Correcting for the dip of the fault leads to the prediction that the 780°C isotherm lay at a depth of ∼7 km relative to the floor of the axial valley (Figure 5a). Given the U-Pb zircon crystallization ages for samples from Hole U1309D are roughly constant (1.20 ± 0.3 Ma) regardless of depth in the hole, this predicts that the 780°C isotherm was locally normal to the fault.

[41] Figure 5 presents the resulting model of the thermal structure for Atlantis Massif at 0.80 Ma while the footwall was still moving and at 0.42 Ma when the fault slip ceased. The depth of the intermediate isotherms (580°C, 450°C, and 300°C) between the U-Pb zircon (780°C) and (U-Th)/He zircon (190°C) isotherms were determined using the age differences between these temperatures

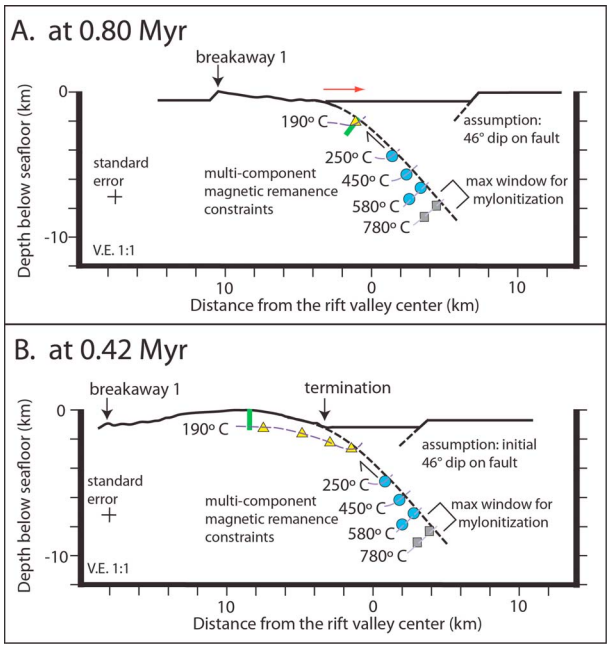

Figure 5. Schematic cross-sections showing the thermal structure of Atlantis Massif OCC (along A-A′ on Figure 2) using the breakaway 1 of *Canales et al.* [2008]. The vertical green line indicates the location of IODP Hole U1309D in relation to the detachment fault breakaway and termination. Grey squares indicate the temperature/depth constraints provided by the U-Pb zircon ages and Ti-in-zircon temperatures which constrain the minimum depth of intrusion, assuming an initial 46° fault dip [*Morris et al.*, 2009]. Blue dots indicate constraints on intermediate temperatures using multi-component magnetic remanence data [*Morris et al.*, 2009] paired with chrons from *Ogg and Smith* [2004]. Yellow triangles indicate constraints on the 190°C isotherm from the new (U-Th)/He ages and closure temperatures. Maximum window for mylonitization (assuming wet plagioclase) in gabbroic rocks is ∼650 to 900°C [*John and Cheadle*, 2010]. (a) At 0.80 Myr, when the upper part of the core just passed through the He closure temperature (see Figure 3c). (b) At 0.42 Myr, when slip on the detachment fault ceased.

shown by the cooling curves in Figure 4, assuming a constant slip rate of 20 mm/yr. Rocks hosted in IODP Hole U1309D cooled through the Curie temperature (∼580°C) by 1.14 Ma, equating to a distance of 1.2 km from the 780°C isotherm corresponding to the U-Pb age of 1.2 Ma. Samples in the core above 1100 mbsf (Figure 4) cooled to 450°C by 1.08 Ma, equivalent to a distance of 1.2 km from the 580°C isotherm. Finally, the two most shallow samples cooled to 250°C by 0.99 Ma (Figure 4), corresponding to a distance of 1.8 km from the 450°C isotherm. These data show that the gabbros cooled relatively quickly to ∼250°C based on the compression of the high temperature isotherms (Figure 5).

[42] Using a similar procedure, we can determine the geometry of the 190°C isotherm during denudation of the fault relative to the reference point of this isotherm, on the fault plane, 1 km below the seafloor at 0.70 Ma. Figure 3c shows that (U-Th)/He ages young with depth, leading to the prediction that the 190°C isotherm is somewhat depressed parallel to the fault plane (Figure 5b).

[43] Our model (Figure 5b) is consistent with the 7 km depth of detachment faulting predicted by *Grimes et al.* [2011] based on one surface sample (Alvin dive sample 3646–1205) from 37 m below the detachment fault surface at Atlantis Massif. The only difference is that *Grimes et al.* [2011] predicted a higher Ti-in-zircon temperature for this sample, partly because of differing zircon titanium concentrations.

[44] The model we present in Figure 5 uses our best estimates of slip rate and fault geometry. Given the thermochronological data of *Grimes et al.* [2008], it is unlikely that the detachment fault slipped at a time averaged rate of less than 20 mm/yr. Using a faster slip rate of 24 mm/yr, corresponding to the full spreading rate of the MAR at this location, would increase depths to the various isotherms by 20%, but leave the geometry of the thermal structure unchanged. For example, by using this faster spreading rate, the depth of the 780°C isotherm would increase from 7 km to 8.4 km. The paleomagnetic data of *Morris et al.* [2009] constrain the dip of the fault to be 46 ± 6° at the depth of the 580°C isotherm. Using the limits of this dip estimate to recalculate the depths of the isotherms adds an uncertainty of ±8% corresponding to a ± 0.6 km uncertainty of the depth of the 780°C isotherm. Again the overall geometry of the thermal structure of the footwall would be unchanged.

5.4. Implications for Hydrothermal Circulation

[45] The location of hydrothermal vents in the hanging wall of a detachment fault at the basalt-hosted TAG hydrothermal field [*deMartin et al.*, 2007] confirms the probable importance of detachment faults as conduits for hydrothermal fluid circulation [*McCaig et al.*, 2007]. *McCaig et al.* [2010] speculate that hydrothermal fluids may reach depths of 7 km below the seafloor and enter into, and cool, the deeper parts of the fault zone, but as they flow upwards, they buffer temperatures and slow cooling

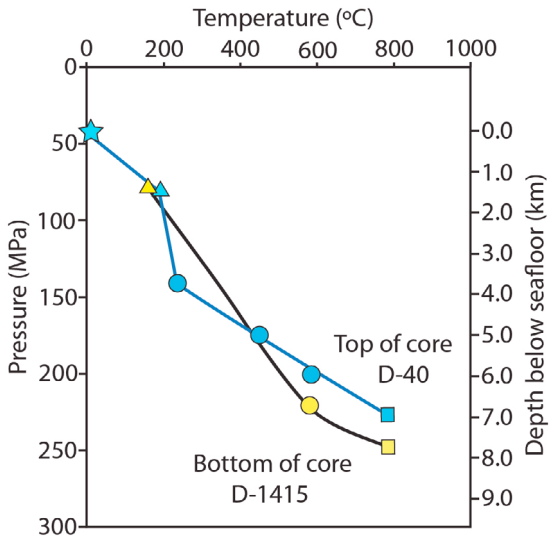

Figure 6. Temperature versus pressure/depth below the seafloor diagram for two depths within IODP Hole U1309D during denudation of the Atlantis Massif oceanic core complex. The pressure is referenced to sea level and thus includes the contribution of seawater residing above the seafloor; whereas the depth show on the right hand side of the plot is referenced to the seafloor. The shape of the symbols correlate with those used to define the location of the isotherms in Figure 5b: blue symbols are for 40 m depth and yellow symbols for 1415 m depth in the core; squares correspond to Ti-in-zircon temperatures (780°C); filled circles correspond to multicomponent magnetic remanence data (580°C, 450°C, and 250°C); triangles correspond to He closure temperatures (190°C), and the star corresponds to the present-day temperature. The thin blue line represents the advective cooling path of a sample from 40 m below the top of IODP Hole U1309D and the thin black line represents the advective cooling path of a sample from the bottom of U1309D.

within the detachment fault zone. Figure 4 shows that the sample nearest to the detachment fault at 40 mbsf in IODP Hole U1309D initially cools rapidly, but subsequently undergoes slow or buffered cooling between ~250°C and 190°C.

[46] Figure 6 shows cooling trajectories for this sample and another from 1415 mbsf as the footwall is uplifted by slip on the detachment fault. The 40 m depth trajectory shows relatively rapid cooling from 580°C at ~6 km below seafloor (bsf) (200 MPa) to 250°C at ~3.75 km bsf (150 MPa), followed by slower cooling to 190°C at ~1.5 km bsf (80 MPa), and final rapid cooling as the footwall reaches the seafloor. The cooling trajectory for sample D-1415 is more uniform with a relatively constant cooling rate. We suggest that the slower cooling interval shown by the sample from 40 mbsf is consistent with efficient hydrothermal convection from 1.5 to 4 km below the axial valley leading to buffering of the fault zone temperature so that it remains relatively constant at 200–250°C over this depth interval. This result implies that the Atlantis Massif detachment fault may have sourced 250°C hydrothermal vents in its hanging wall and is similar, although less extreme, to the model for hydrothermal circulation along detachment faults proposed by *McCaig et al.* [2010].

[47] Consequently, our model for the thermal structure of the Atlantis Massif OCC, which shows apparent compression of the high temperature (250°C to 780°C) isotherms at depth (Figure 5b) is consistent with hydrothermal flow along the upper part (<4 km) of the active detachment fault. The observation that the five uppermost samples from IODP Hole U1309D have similar (U-Th)/He ages and come from a zone of pervasive greenschist facies alteration while samples from below 800 m have younger (U-Th)/He ages (Figure 3c) and lie in a less altered zone argues that hydrothermal flow extended into the upper 800 m of the footwall.

5.5. Geologic Implications

[48] Estimated temperatures for the solidus of oceanic gabbro using amphibole-plagioclase thermometry are 860 ± 30°C [*Coogan et al.*, 2001]. The 780°C isotherm deduced from the Ti-in-zircon temperatures reported in this study likely corresponds to the transition between semi-brittle/ductile faulting and magmatic flow at the margins of any magma chamber. Our conclusion that the 780°C isotherm resides ~7 km below the floor of the axial valley constrains the maximum depth of detachment faulting (and likely earthquake generation) and the upper limit of significant gabbro emplacement and final crystallization. This depth is also consistent with the work of *deMartin et al.* [2007] who show earthquake hypocenters from microseismicity at depths between 3 and 7 km beneath the TAG hydrothermal field at 26°N on the MAR.

[49] Compression of the high temperature (>580°C) isotherms in our model (Figure 5b) supports the suggestion of *John and Cheadle* [2010] of a very narrow temperature window available for the formation of mylonitic rocks associated with the detachment fault system in OCCs. They argued that for gabbroic rocks with wet plagioclase, plastic deformation can occur at temperatures between 600°C and 900°C. In contrast, for gabbroic rocks with dry plagioclase, plastic deformation can only occur above ~850°C [*John and Cheadle*, 2010]. The model in

Figure 5b suggests that mylonitic rocks would form at Atlantis Massif, only if plagioclase is wet, and then only in a narrow 1 km thick window above the 600°C isotherm. This result is consistent with the observation that at IODP Hole U1309D, crystal plastic deformation is scarce [*Blackman et al.*, 2011].

[50] The prediction that the present-day 190°C isotherm currently resides between 1400 and 2000 mbsf (Figure 3c) suggests that the temperature at Moho depths (4.5 to 5 km), as suggested by the seismic tomographic studies of *Blackman and Collins* [2010] is >500°C. This result has profound implications for the possibility of drilling the Moho at the Atlantis Massif OCC.

6. Conclusions

[51] Combined U-Pb zircon chronometry, Ti-in-zircon thermometry, multicomponent magnetic remanence studies, and (U-Th)/He zircon thermochronometry (and closure temperatures), have led to a new model for the thermal structure of the uppermost 1.4 km of the Atlantis Massif OCC during active seafloor spreading and associated detachment faulting.

[52] We have shown:

[53] 1. The uppermost 800 m of IODP Hole U1309D cooled rapidly from ~780°C to ~250°C at mean rates of 2895 (+1276/−1162) °C Myr^{-1}, while the lowermost 600 m of U1309D cooled at slower mean rates of ~500 (+125/−102) °C Myr^{-1} from ~780°C to present-day temperatures.

[54] 2. The depth to the semi-brittle root of the detachment fault is ~7 km below the axial valley, assuming a time-averaged fault slip rate of 20 mm/yr, and a rolling hinge model for the fault sub-surface geometry. This depth also likely corresponds to the uppermost depth at which large gabbro bodies were emplaced into the footwall of the detachment fault.

[55] 3. The thermal structure, cooling history, and extensive greenschist facies alteration of the upper part of the footwall is consistent with hydrothermal flow within the top 800 m of the footwall and to depths of ~4 km below the seafloor along the fault. A reduced cooling rate of ~300°C Myr^{-1} between ~250°C and 190°C suggests that hydrothermal convection buffered cooling of the of the uppermost footwall over this temperature range.

[56] 4. The present-day 190°C isotherm currently resides between 1400 and 2000 mbsf, suggesting that the temperature at Moho depths (4.5 to 5 km [*Blackman and Collins*, 2010]) is >500°C.

Acknowledgments

[57] This research used samples and data provided by the Integrated Ocean Drilling Program (IODP). Technical assistance from both Stefan Nicolescu and Uttam Chowdhury in obtaining (U-Th)/He zircon ages at ARHDL is gratefully acknowledged. Funding for this project came from: NSF Grant OCE-0550456 (John), OCE-0550466 (Gee), GSA Graduate Student Research Grant (9288–10) to Schoolmeesters, and Wyoming NASA Space Grant Consortium Graduate Research Fellowship NNG05G165H to Schoolmeesters. Comments and reviews by Gary Axen, Nick Hayman, Thorsten Becker, as well as an unnamed reviewer and associate editor were all of value for improving the manuscript.

References

Baines, A. G., M. J. Cheadle, B. E. John, and J. J. Schwartz (2008), The rate of oceanic detachment faulting at Atlantis Bank, SW Indian Ridge, *Earth Planet. Sci. Lett.*, *273*, 105–114, doi:10.1016/j.epsl.2008.06.013.

Blackman, D. K., and J. A. Collins (2010), Lower crustal variability and the crust/mantle transition at the Atlantis Massif oceanic core complex, *Geophys. Res. Lett.*, *37*, L24303, doi:10.1029/2010GL045165.

Blackman, D. K., J. R. Cann, B. Janssen, and D. K. Smith (1998), Origin of extensional core complexes: Evidence from the Mid-Atlantic Ridge at Atlantis Fracture Zone, *J. Geophys. Res.*, *103*, 21,315–21,333, doi:10.1029/98JB01756.

Blackman, D. K., et al. (2002), Geology of the Atlantis Massif (Mid-Atlantic Ridge, 30°N): Implications for the evolution of an ultramafic oceanic core complex, *Mar. Geophys. Res.*, *23*, 443–469, doi:10.1023/B:MARI.0000018232.14085.75.

Blackman, D. K., B. Ildefonse, B. E. John, Y. Ohara, D. J. Miller, C. J. MacLeod, and the Expedition 304/305 Scientists (2006), *Oceanic Core Complex Formation, Atlantis Massif*, *Proc. Integr. Ocean Drill. Program*, *304*, doi:10.2204/iodp.proc.304305.2006.

Blackman, D. K., et al. (2011), Drilling constraints on lithospheric accretion and evolution at Atlantis Massif, Mid-Atlantic Ridge 30°N, *J. Geophys. Res.*, *116*, B07103, doi:10.1029/2010JB007931.

Boschi, C., G. L. Fruh-Green, A. Delacour, J. A. Karson, and D. S. Kelley (2006), Mass transfer and fluid flow during detachment faulting and development of an oceanic core complex, Atlantis Massif (MAR 30°N), *Geochem. Geophys. Geosyst.*, *7*, Q01004, doi:10.1029/2005GC001074.

Buck, W. R. (1988), Flexural rotation of normal faults, *Tectonics*, *7*, 959–973, doi:10.1029/TC007i005p00959.

Buck, W. R., L. L. Lavier, and A. N. B. Poliakov (2005), Modes of faulting at mid-ocean ridges, *Nature*, *434*, 719–723, doi:10.1038/nature03358.

Canales, J. P., R. A. Sohn, and B. J. deMartin (2007), Crustal structure of the Trans-Atlantic Geotraverse (TAG) segment (Mid-Atlantic Ridge, 26°10′N): Implications for the nature of hydrothermal circulation and detachment faulting at slow spreading ridges, *Geochem. Geophys. Geosyst.*, *8*, Q08004, doi:10.1029/2007GC001629.

Canales, J. P., B. E. Tucholke, M. Xu, J. A. Collins, and D. L. DuBois (2008), Seismic evidence for large-scale compositional heterogeneity of oceanic core complexes, *Geochem. Geophys. Geosyst.*, *9*, Q08002, doi:10.1029/2008GC002009.

Cann, J. R., D. K. Blackman, D. K. Smith, E. McAllister, B. Janssen, S. Mello, E. Avgerinos, A. R. Pascoe, and J. Escartín (1997), Corrugated slip surfaces formed at ridge-transform intersections on the Mid-Atlantic Ridge, *Nature*, *385*, 329–332, doi:10.1038/385329a0.

Cherniak, D. J., and E. B. Watson (2003), Diffusion in zircon, in *Zircon*, *Rev. Mineral. Geochem.*, vol. 53, edited by J. M. Hanchar and P. W. O. Hoskin, pp. 113–143, Mineral. Soc. of Am., Washington, D. C.

Coogan, L. A., R. N. Wilson, K. M. Gillis, and C. J. MacLeod (2001), Near-solidus evolution of oceanic gabbros: Insights from amphibole geochemistry, *Geochim. Cosmochim. Acta*, *65*, 4339–4357, doi:10.1016/S0016-7037(01)00714-1.

Crittenden, M. D., P. J. Coney, and G. H. Davis (1980), Cordilleran metamorphic core complexes, *Mem. Geol. Soc. Am.*, *153*, 490.

Davis, G. A., and G. S. Lister (1988), Detachment faulting in continental extension: Perspectives from the Southwestern U.S. Cordillera, in *Processes in Continental Lithospheric Deformation*, edited by S. P. Clark et al., *Spec. Pap. Geol. Soc. Am.*, *218*, 133–159.

deMartin, B. J., R. A. Sohn, J. P. Canales, and S. E. Humphris (2007), Kinematics and geometry of active detachment faulting beneath the Trans-Atlantic Geotraverse (TAG) hydrothermal field on the Mid-Atlantic Ridge, *Geology*, *35*, 711–714, doi:10.1130/G23718A.1.

Dick, H. J. B., M. A. Tivey, and B. E. Tucholke (2008), Plutonic foundation of a slow-spreading ridge segment: Oceanic core complex at Kane Megamullion, 23°30′N, 45°20′W, *Geochem. Geophys. Geosyst.*, *9*, Q05014, doi:10.1029/2007GC001645.

Dodson, M. H. (1973), Closure temperature in cooling geochronological and petrological systems, *Contrib. Mineral. Petrol.*, *40*, 259–274, doi:10.1007/BF00373790.

Drouin, M., M. Godard, B. Ildefonse, O. Bruguier, and C. J. Garrido (2009), Geochemical and petrographic evidence for magmatic impregnation in the oceanic lithosphere at Atlantis Massif, Mid-Atlantic Ridge (IODP Hole U1309D, 30°N), *Chem. Geol.*, *264*, 71–88, doi:10.1016/j.chemgeo.2009.02.013.

Drouin, M., B. Ildefonse, and M. Godard (2010), A microstructural imprint of melt impregnation in slow spreading lithosphere: Olivine-rich troctolites from the Atlantis Massif, Mid-Atlantic Ridge, 30°N, IODP Hole U1309D, *Geochem. Geophys. Geosyst.*, *11*, Q06003, doi:10.1029/2009GC002995.

Escartín, J., and J. P. Canales (2011), Detachments in oceanic lithosphere: Deformation, magmatism, fluid flow, and ecosystems, *Eos Trans. AGU*, *92*(4), 31, doi:10.1029/2011EO040003.

Expedition 340 T Scientists (2012), Atlantis Massif Oceanic Core Complex: Velocity, porosity, and impedance contrasts within the domal core of Atlantis Massif: Faults and hydration of lithosphere during core complex evolution, *Prelim. Rep. Integrated Ocean Drill. Program*, *340T*, doi:10.2204/iodp.pr.340T.2012.

Farley, K. A., R. A. Wolf, and L. T. Silver (1996), The effects of long alpha-stopping distances on (U-Th)/He ages, *Geochim. Cosmochim. Acta*, *60*, 4223–4229, doi:10.1016/S0016-7037(96)00193-7.

Ferriss, E. D. A., E. J. Essene, and U. Becker (2008), Computational study of the effect of pressure on the Ti-in-zircon geothermometer, *Eur. J. Mineral.*, *20*, 745–755, doi:10.1127/0935-1221/2008/0020-1860.

Ferry, J. M., and E. B. Watson (2007), New thermodynamic models and revised calibrations for the Ti-in-zircon and Zr-in-rutile thermometers, *Contrib. Mineral. Petrol.*, *154*, 429–437, doi:10.1007/s00410-007-0201-0.

Froitzheim, N., and G. Manatschal (1996), Kinematics of Jurassic rifting, mantle exhumation and passive-margin formation in the Austroalpine and Penninic nappes (eastern Switzerland), *Geol. Soc. Am. Bull.*, *108*, 1120–1133, doi:10.1130/0016-7606(1996)108<1120:KOJRME>2.3.CO;2.

Fu, B., F. Z. Page, A. J. Cavosie, J. Fournelle, N. T. Kita, J. S. Lackey, S. A. Wilde, and J. W. Valley (2008), Ti-in-zircon thermometry: Applications and limitations, *Contrib. Mineral. Petrol.*, *156*, 197–215, doi:10.1007/s00410-008-0281-5.

Garcés, M., and J. S. Gee (2007), Paleomagnetic evidence of large footwall rotations associated with low-angle faults at the Mid-Atlantic Ridge, *Geology*, *35*, 279–282, doi:10.1130/G23165A.1.

Gee, J., and W. P. Meurer (2002), Slow cooling of middle and lower oceanic crust inferred from multicomponent magnetization of gabbroic rocks from the Mid-Atlantic Ridge south of the Kane fracture zone (MARK) area, *J. Geophys. Res.*, *107*(B7), 2137, doi:10.1029/2000JB000062.

Grimes, C. B., B. E. John, M. J. Cheadle, and J. L. Wooden (2008), Protracted construction of gabbroic crust at a slow spreading ridge: Constraints from $^{206}Pb/^{238}U$ zircon ages from Atlantis Massif and IODP Hole U1309D (30°N, MAR), *Geochem. Geophys. Geosyst.*, *9*, Q08012, doi:10.1029/2008GC002063.

Grimes, C. G., B. E. John, M. J. Cheadle, F. K. Mazdab, J. L. Wooden, S. Swapp, and J. J. Schwartz (2009), On the occurrence, trace element geochemistry, and crystallization history of zircon from in situ ocean lithosphere, *Contrib. Mineral. Petrol.*, *158*, 757–783, doi:10.1007/s00410-009-0409-2.

Grimes, C. B., M. J. Cheadle, B. E. John, P. W. Reiners, and J. L. Wooden (2011), Cooling rates and the depth of detachment faulting at oceanic core complexes: Evidence from zircon Pb/U and U-Th/He ages, *Geochem. Geophys. Geosyst.*, *12*, Q0AG01, doi:10.1029/2010GC003391.

Guenthner, W., P. W. Reiners, R. A. Ketcham, and L. Nasdala (2011), Development of a radiation damage and annealing model for the zircon (U-Th)/He thermochronometer, Abstract V23A-2550 presented at 2011 Fall Meeting, AGU, San Francisco, Calif., 5–9 Dec.

Hanchar, J. M., and C. F. Miller (1993), Zircon zonation patterns as revealed by cathodoluminescence and backscattered electron images: Implications for interpretation of complex crustal histories, *Chem. Geol.*, *110*, 1–13, doi:10.1016/0009-2541(93)90244-D.

Hansen, L. N., M. J. Cheadle, B. E. John, S. M. Swapp, H. J. B. Dick, B. E. Tucholke, and M. A. Tivey (2007), Styles of detachment faulting at the Kane Oceanic Core Complex, 23°N Mid-Atlantic Ridge, *Eos Trans. AGU*, *88*(52), Fall Meet. Suppl., Abstract T51F-07.

Hourigan, J. K., P. W. Reiners, and M. T. Brandon (2005), Zonation-dependent alpha-ejection in (U-Th)/He chronometry, *Geochim. Cosmochim. Acta*, *69*, 3349–3365, doi:10.1016/j.gca.2005.01.024.

Ildefonse, B., D. K. Blackman, B. E. John, Y. Ohara, D. J. Miller, C. J. MacLeod, and the Integrated Ocean Drilling Program Expeditions 304/305 Science Party (2007), Oceanic core complexes and crustal accretion at slow spreading ridges, *Geology*, *35*, 623–626, doi:10.1130/G23531A.1.

John, B. E. (1987), Geometry and evolution of a mid-crustal extensional fault system: Chemehuevi Mountains, southeastern California, in *Continental extensional tectonics*, edited by M. P. Coward, J. F. Dewey, and P. L. Hancock, *Geol. Soc. Spec. Publ.*, *28*, 313–335.

John, B. E., and M. J. Cheadle (2010), Deformation and alteration associated with oceanic and continental detachment fault systems: Are they similar?, in *Diversity of Hydrothermal Systems on Slow Spreading Ocean Ridges*, *Geophys. Monogr. Ser.*, vol. 188, edited by P. A. Rona et al., pp. 175–205, AGU, Washington, D. C., doi:10.1029/2008GM000772.

John, B. E., M. J. Cheadle, J. S. Gee, C. B. Grimes, A. Morris, and N. Pressling (2009), Data report: Spatial and temporal evolution of slow-spread oceanic crust—Graphic sections of core recovered from IODP Hole U1309D, Atlantis Massif, 30°N, MAR (including Pb/U zircon geochronology and magnetic remanence data), in *Oceanic Core Complex Formation, Atlantis Massif*, *Proc. Integr. Ocean Drill. Program*, *304/305*, doi:10.2204/iodp.proc.304305.205.2009.

Karson, J. A., G. L. Fruh-Green, D. S. Kelley, E. A. Williams, D. R. Yoerger, and M. Jakuba (2006), Detachment shear zone of the Atlantis Massif core complex, Mid-Atlantic Ridge, 30°N, *Geochem. Geophys. Geosyst.*, *7*, Q06016, doi:10.1029/2005GC001109.

Kelemen, P. B., E. Kikawa, and D. J. Miller, and the Shipboard Scientific Party (2007), Leg 209 summary: Processes in a 20-km-thick conductive boundary layer beneath the Mid-Atlantic Ridge, 14°–16°N, *Proc. Ocean Drill. Program Sci. Results*, *209*, 1–33, doi:10.2973/odp.proc.sr.209.001.2007.

Kelley, D. S., et al. (2001), An off-axis hydrothermal vent field discovered near the Mid-Atlantic Ridge at 30°N, *Nature*, *412*, 145–149, doi:10.1038/35084000.

Kong, L. S. L., S. C. Solomon, and G. M. Purdy (1992), Microearthquake characteristics of a mid-ocean ridge along-axis high, *J. Geophys. Res.*, *97*, 1659–1685, doi:10.1029/91JB02566.

Maclennan, J., T. Hulme, and S. C. Singh (2005), Cooling of the lower oceanic crust, *Geology*, *33*, 357–360, doi:10.1130/G21207.1.

MacLeod, C. J., R. C. Searle, B. J. Murton, J. F. Casey, C. Mallows, S. C. Unsworth, K. L. Achenbach, and M. Harris (2009), Life cycle of oceanic core complexes, *Earth Planet. Sci. Lett.*, *287*, 333–344, doi:10.1016/j.epsl.2009.08.016.

MacLeod, C. J., J. Carlut, J. Escartín, H. Horen, and A. Morris (2011), Quantitative constraint on footwall rotations at the 15°45′N oceanic core complex, Mid-Atlantic Ridge: Implications for oceanic detachment fault processes, *Geochem. Geophys. Geosyst.*, *12*, Q0AG03, doi:10.1029/2011GC003503.

McCaig, A. M., R. A. Cliff, J. Escartín, A. E. Fallick, and C. J. MacLeod (2007), Oceanic detachment faults focus very large volumes of black smoker fluids, *Geology*, *35*, 935–938, doi:10.1130/G23657A.1.

McCaig, A. M., A. Delacour, A. F. Fallick, T. Castelain, and G. L. Fruh-Green (2010), Detachment fault control on hydrothermal circulation systems: Interpreting the subsurface beneath the TAG hydrothermal field using the isotopic and geological evolution of oceanic core complexes in the Atlantic, in *Diversity of Hydrothermal Systems on Slow Spreading Ocean Ridges*, *Geophys. Monogr. Ser.*, vol. 188, edited by P. A. Rona et al., pp. 207–239, AGU, Washington, D. C., doi:10.1029/2008GM000729.

Morris, A., J. S. Gee, N. Pressling, B. E. John, C. J. MacLeod, C. B. Grimes, and R. C. Searle (2009), Footwall rotation in an oceanic core complex quantified using reoriented Integrated Ocean Drilling Program core samples, *Earth Planet. Sci. Lett.*, *287*, 217–228, doi:10.1016/j.epsl.2009.08.007.

Morris, A., N. Pressling, and J. S. Gee (2011), Palaeomagnetic constraints on the evolution of the Atlantis Massif oceanic core complex (Mid-Atlantic Ridge, 30°N), Abstract T23D-2424 presented at 2011 Fall Meeting, AGU, San Francisco, Calif., 5–9 Dec.

Ogg, J. G., and A. G. Smith (2004), The geomagnetic polarity time scale, in *A Geological Time Scale 2004*, edited by F. M. Gradstein, J. G. Ogg, and A. G. Smith, pp. 63–86, Cambridge Univ. Press, Cambridge, U. K.

Ohara, Y., T. Yoshida, Y. Kato, and S. Kasuga (2001), Giant megamullion in the Parece Vela backarc basin, *Mar. Geophys. Res.*, *22*, 47–61, doi:10.1023/A:1004818225642.

Okino, K., K. Matsuda, D. M. Christie, Y. Nogi, and K. Koizumi (2004), Development of oceanic detachment and asymmetric spreading at the Australian-Antarctic Discordance, *Geochem. Geophys. Geosyst.*, *5*, Q12012, doi:10.1029/2004GC000793.

Olive, J. A., M. D. Behn, and B. E. Tucholke (2010), The structure of oceanic core complexes controlled by the depth distribution of magma emplacement, *Nat. Geosci.*, *3*, 491–495, doi:10.1038/ngeo888.

Phipps Morgan, J., and Y. J. Chen (1993), Dependence of ridge-axis morphology on magma supply and spreading rate, *Nature*, *364*, 706–708, doi:10.1038/364706a0.

Reiners, P. W. (2005), Zircon (U-Th)/He thermochronometry, in *Low Temperature Thermochronometry*, *Rev. Mineral. Geochem.*, vol. 58, edited by P. W. Reiners and T. A. Ehlers, pp. 151–179, Mineral. Soc. of Am., Washington, D. C.

Reiners, P. W., K. A. Farley, and H. J. Hickes (2002), He diffusion and (U-Th)/He thermochronometry of zircon: Initial results from Fish Canyon Tuff and Gold Butte, *Tectonophysics*, *349*, 297–308, doi:10.1016/S0040-1951(02)00058-6.

Reiners, P. W., T. L. Spell, S. Nicolescu, and K. A. Zanetti (2004), Zircon (U-Th)/He thermochronometry: He diffusion and comparisons with $^{40}Ar/^{39}Ar$ Dating, *Geochim. Cosmochim. Acta*, *68*, 1857–1887, doi:10.1016/j.gca.2003.10.021.

Reiners, P. W., S. N. Thomson, D. McPhilips, R. A. Donelick, and J. J. Roering (2007), Wildfire thermochronology and the fate and transport of apatite in hillslope and fluvial environments, *J. Geophys. Res.*, *112*, F04001, doi:10.1029/2007JF000759.

Schouten, H., D. K. Smith, J. R. Cann, and J. Escartín (2010), Tectonic versus magmatic extension in the presence of core complexes at slow-spreading ridges from a visualization of faulted seafloor topography, *Geology*, *38*, 615–618, doi:10.1130/G30803.1.

Schroeder, T., and B. E. John (2004), Strain localization on an oceanic detachment fault system, Atlantis Massif, 30°N, Mid-Atlantic Ridge, *Geochem. Geophys. Geosyst.*, *5*, Q11007, doi:10.1029/2004GC000728.

Small, C. (1998), Global systematics of mid-ocean ridge morphology, in *Faulting and Magmatism at Mid-Ocean Ridges*, vol. 106, edited by W. R. Buck et al., pp. 1–25, AGU, Washington, D. C., doi:10.1029/GM106p0001.

Smith, D. K., J. R. Cann, and J. Escartín (2006), Widespread active detachment faulting and core complex formation near 13°N on the Mid-Atlantic Ridge, *Nature*, *442*, 440–443, doi:10.1038/nature04950.

Smith, D. K., J. Escartín, H. Schouten, and J. R. Cann (2008), Fault rotation and core complex formation: Significant processes in seafloor formation at slow-spreading mid-ocean ridges (Mid-Atlantic Ridge, 13°–15°N), *Geochem. Geophys. Geosyst.*, *9*, Q03003, doi:10.1029/2007GC001699.

Stockli, D. F. (2005), Application of low-temperature thermochronometry to extensional tectonic settings, in *Low Temperature Thermochronometry*, *Rev. Mineral. Geochem.*, vol. 58, edited by P. W. Reiners and T. A. Ehlers, pp. 411–448, Mineral. Soc. of Am., Washington, D. C., doi:10.2138/rmg.2005.58.16.

Tani, K., D. J. Dunkley, and Y. Ohara (2011), Termination of backarc spreading: Zircon dating of a giant oceanic core complex, *Geology*, *39*, 47–50.

Toomey, D. R., S. C. Solomon, G. M. Purdy, and M. H. Murray (1985), Microearthquakes beneath the Median Valley of the Mid-Atlantic Ridge near 23°N: Hypocenters and focal mechanisms, *J. Geophys. Res.*, *90*(B7), 5443–5458, doi:10.1029/JB090iB07p05443.

Toomey, D. R., S. C. Solomon, and G. M. Purdy (1988), Microearthquakes beneath Median Valley of Mid-Atlantic Ridge near 23°N: Tomography and tectonics, *J. Geophys. Res.*, *93*(B8), 9093–9112, doi:10.1029/JB093iB08p09093.

Tucholke, B. E., and J. Lin (1994), A geological model for the structure of ridge segments in slow spreading ocean crust, *J. Geophys. Res.*, *99*, 11,937–11,958, doi:10.1029/94JB00338.

Tucholke, B. E., J. Lin, and M. C. Kleinrock (1998), Megamullions and mullion structure defining oceanic metamorphic core complexes on the Mid-Atlantic Ridge, *J. Geophys. Res.*, *103*, 9857–9866, doi:10.1029/98JB00167.

Tucholke, B. E., M. D. Behn, W. R. Buck, and J. Lin (2008), Role of melt supply in oceanic detachment faulting and formation of megamullions, *Geology*, *36*, 455–458, doi:10.1130/G24639A.1.

Watson, E. B., D. A. Wark, and J. B. Thomas (2006), Crystallization thermometers for zircon and rutile, *Contrib. Mineral. Petrol.*, *151*, 413–433, doi:10.1007/s00410-006-0068-5.

Wernicke, B., and G. J. Axen (1988), On the role of isostasy in the evolution of normal fault systems, *Geology*, *16*, 848–851.

Wolfe, C. J., G. M. Purdy, D. R. Toomey, and S. C. Solomon (1995), Microearthquake characteristics and crustal velocity structure at 29°N on the Mid-Atlantic Ridge: The architecture of a slow spreading segment, *J. Geophys. Res.*, *100*, 24,449–24,472, doi:10.1029/95JB02399.

Wolfe, M. R., and D. F. Stockli (2010), Zircon (U-Th)/He thermochronometery in the KTB drill hole, Germany, and its implications for bulk He diffusion kinetics in zircon, *Earth Planet. Sci. Lett.*, *295*, 69–82, doi:10.1016/j.epsl.2010.03.025.

Zervas, C. E., J. C. Sempere, and J. Lin (1995), Morphology and crustal structure of a small transform fault along the Mid-Atlantic Ridge: The Atlantis Fracture Zone, *Mar. Geophys. Res.*, *17*, 275–300, doi:10.1007/BF01203466.